Forschung im Ingenieurwesen (2025)89:46
https://doi.org/10.1007/s10010-025-00794-2

ORIGINALARBEITEN/ORIGINALS

Design of a TFF critical testing gear set under reverse bending

Johannes Rolzhäuser[1] · **Dieter Mevissen**[1] · **Christian Brecher**[1]

Received: 15 September 2024 / Accepted: 30 January 2025

Abstract

This report deals with the macro geometric design of a gear set for investigating the influence of reverse loading on the tooth flank fracture load capacity. Due to power density increase of gearboxes in the past, gears are becoming more and more subject to interior fatigue, since the tribological system as well as the material in the surface zone have been optimized continuously over the years. The influence of reverse loading on the tooth flank fracture load capacity is currently only known to a limited extent in research work. An FE-based approach for calculating the tooth flank fracture load capacity was therefore extended to include the influence of the reverse loading. In an initial analysis, the load capacity reducing influence of the reverse bending load on the tooth flank fracture load capacity has been simulated. Building on this, the present work addresses a more detailed analysis about the influence of the selected stress hypothesis and the influence of the macro geometry. The aim is, to find a gear design that reacts as sensitive as possible to an applied reverse bending load regarding the risk of tooth flank fracture. Finally, the robustness regarding a modification in hardness and residual stress curve is investigated.

Auslegung einer zahnflankenbruchkritischen Prüfverzahnung unter Biegewechsellast

Zusammenfassung

Als Folge der Optimierung der letzten Jahre treten vermehrt Zahnflankenbrüche und innere Zahnermüdungsbrüche auf, welche ihren Rissausgang im Zahnvolumen unterhalb der gehärteten Randschicht haben. Zum Einfluss einer wechselnden Beanspruchung (Biegewechsellast) auf die Zahnflankenbruchtragfähigkeit finden sich derzeit nur wenig Erkenntnisse. Am WZL der RWTH Aachen wurde daher der FE-basierte Ansatz zur Berechnung der Zahnflankenbruchtragfähigkeit um den Einfluss der Biegewechsellast erweitert. In einer ersten Analyse wurde anschließend der tragfähigkeitsmindernde Einfluss der Biegewechsellast auf die Zahnflankenbruchtragfähigkeit simulativ gezeigt. Darauf aufbauend wurde in der vorliegenden Arbeit eine tiefergehende Analyse im Hinblick auf den Einfluss der gewählten Vergleichsspannungshypothese sowie den Einfluss der Makrogeometrie durchgeführt. Zur Auslegung einer Prüfverzahnungsgeometrie wurde eine Makrogeometrievariation durchgeführt und die Anstrengungstiefenverläufe für unidirektionale und bidirektionale Belastung verglichen. Hier zeigt sich, dass vor allem der Querschub für die Tragfähigkeitsreduktion bei Biegewechsellast relevant ist. Somit kann der Normalzahndicke ein übergeordneter Einfluss auf den Tragfähigkeitsabfall durch anliegende Biegewechsellast beigemessen werden. Der Tragfähigkeitsabfall ist mit den gewählten Randbedingungen umso größer, je höher die Einsatzhärtetiefe gewählt wird. Die Festlegung der Einsatzhärtetiefe einer Verzahnung setzt also die Kenntnis des makrogeometrischen Einflusses der Biegewechsellast auf die Zahnflankenbruchtragfähigkeit voraus.

1 Introduction

As a consequence of the constant increase in the power density of gearboxes, new types of damages are increasingly coming to the fore in gear design. The progressive optimization of the tooth flank and tooth root load capacity in the near-surface area, e.g. through ultra-fine grinding, shot peening or highly additive lubricants, is leading to a shift in

---

✉ Johannes Rolzhäuser
j.rolzhaeuser@wzl.rwth-aachen.de

[1] Laboratory for Machine Tools and Production Engineering (WZL), RWTH Aachen University, Campus Boulevard 30, 52074 Aachen, Germany

crack initiation from the surface to higher material depths [1]. As a result, tooth flank fractures (TFF: Tooth Flank Fracture) and tooth interior fatigue fractures (TIFF: Tooth Interior Fatigue Fracture) occur more frequently, which result from high stress in combination with low strength in the tooth volume. In the last years, research has been carried out to understand the damage mechanism of tooth flank fracture [1–4]. Latest work has focused on the calculation of stress and strength, on the general analysis of influences such as residual stresses and non-metallic inclusions [1–3, 5, 6] as well as the reproduction of the damage pattern in an analogy test [7–9].

Currently, there is little research on the influence of alternating load (reverse bending load) on the tooth flank fracture load capacity, although various studies assume a considerable influence [10–13]. The FE-based approach for calculating the tooth flank fracture load capacity was therefore extended to include the influence of the alternating bending load [14]. In an initial analysis, the load capacity reducing influence of the alternating bending load on the tooth flank fracture load capacity was simulated. Extending this study, the present work addresses a more in-depth analysis with regard to the influence of the selected stress hypothesis and the influence of the macro geometry. The aim is to design a gear set that reacts as sensitive as possible to an applied alternating bending load with regard to the risk of tooth flank fracture. Furthermore, the robustness of the gear design with regard to changes in hardness and residual stresses is investigated.

2 State of the art

For a better prediction and calculation of the risk of tooth flank fracture, the method based on the work of Konowalczyk and Goergen [1, 8] is constantly being further developed. In the state of the art, the damage mechanism “tooth flank fracture” as well as its influencing variables and the approach developed for load capacity calculation are explained in more detail. Subsequently, the state of the art on the influence of the geometry under pulsating and alternating load is discussed in particular.

2.1 Failure mechanism of TFF and TIFF

Tooth flank fracture is a type of fatigue damage that occurs on both spur and bevel gears. A tooth flank fracture is the breakage of a tooth in the area of the active tooth flank. The damage occurs as a result of permanently pulsating or alternating dynamic loads and is caused by repeated overloading in the fatigue strength range [15].

Tooth flank fractures generally originate below the flank surface at approximately twice the case hardening depth $t \approx 2 \cdot CHD_{550}$ or the transition area between the surface and core microstructure at a nonmetallic inclusion [1–3, 16]. The decisive factor for crack initiation is that the defect, in contrast to the surrounding matrix material, has a different young’s modulus, which leads to local stress peaks during engagement [2, 3]. The stress leading to tooth flank fracture is divided into the primary stress due to Hertzian contact and the secondary stress due to bending and transverse shearing [8].

The primary crack grows from the crack starting point at an angle of around 40–50° to the active tooth flank in the direction of the opposing flank, see Fig. 1 (left). In direction of the active flank the crack propagates more slowly, as the crack grows in the hardened surface layer. Secondary and tertiary cracks can also occur, which, according to Witzig, are caused by internal material separation because of the primary crack and the associated local change in stiffness. With increasing number of load cycles, the secondary crack grows roughly parallel to the tooth tip in the direction of the primary crack propagating inside the tooth. Furthermore, tertiary cracks can occur, which have a similar crack pattern to the secondary crack but occur at a different location with regard to the tooth width coordinate. After breaking through the entire surface of the component, a forced fracture of the remaining material and the characteristic material breakout occur within a few load cycles [2].

In addition to the damage type tooth flank fracture, a damage type similar to tooth flank fracture but with different crack growth is observed [10–12, 16]. The tooth interior fatigue fracture can occur at torque ratios $R_M = 0$ and $R_M = -1$ [13]. Intermediate gears subject to alternating loads, e.g. planetary gears, are particularly affected by this type of damage [10, 13]. Figure 1 shows the damage pattern of TFF compared to TIFF.

The influencing variables and crack initiation mechanisms between the two damage types TFF and TIFF are similar. A significant difference between TFF and TIFF is to be mentioned with regard to the crack propagation. Similar to TFF, the crack starts below the flank surface. This fact distinguishes the two types of damage from surface damage and tooth root fractures, where the crack starts growing from the surface. In the case of a TIFF, the crack propagates predominantly in the direction of the core and forms a distinct plateau parallel to the tooth tip, see Fig. 1 (right). As soon as the crack reaches the surface layer, its further progression bends towards the tooth root, allowing the crack to appear at the surface. The higher the plateau within the tooth volume, the narrower the plateau width. This property suggests that the width of the plateau is correlated with the non-hardened core area of the tooth. In particular, this core area becomes narrower as it gets closer to the tooth tip [2, 10–12, 16].

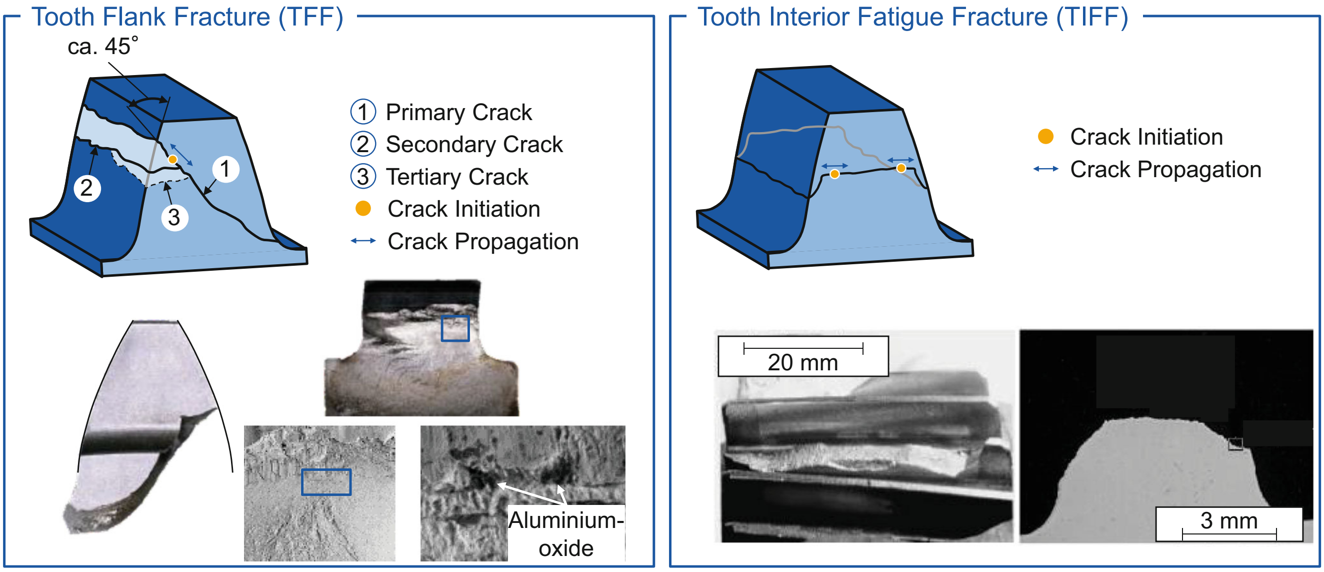

Fig. 1 Comparison of Tooth Flank Fracture and Tooth Interior Fatigue Fracture [1, 11]

Extensive, mainly numerical investigations of the occurrence of TIFF damage were carried out by MackAldener [10–12, 16]. MackAldener considers the tensile residual stresses present in the core after case hardening and the alternating load at $R_M \neq 0$ to be decisive for the initiation of TIFF damages in the tooth interior [10]. He uses Findley's critical plane stress hypothesis as a criterion for crack initiation, while the residual stress depth profile is simulated and calibrated on the basis of measurements [16]. MackAldener calculates a CIRF-factor (CIRF: Crack Initiation Risk Factor) for each node of the FE model for eight discrete rolling positions of the left and right flank in the mesh [16]. For gears subjected to alternating loads, MackAldener calculates a CIRF that is around 20% higher than for gears subjected to purely pulsating load [16]. In a parameter study, Al et al. confirm the computational influence analyses of MackAldener, whereby they use a simple 3D tooth contact analysis instead of a full FE software and rate this as sufficient with regard to the calculation quality [10, 17].

2.2 Factors influencing the tooth flank fracture load capacity

The main factors influencing the tooth flank fracture load capacity are explained below. The focus here are the geometric influencing variables known from the literature, which are relevant for the design of a test gear set that is particularly sensitive to alternating bending loads.

2.2.1 Influencing material factors

Hardness and residual stresses Hardness is considered to have a significant influence on the tooth flank fracture load capacity [1, 2, 8, 9]. The positive influence of an increase in the case hardening depth CHD_{550} on the tooth flank fracture load capacity is highlighted in numerous sources [1, 10, 18–20]. With regard to the choice of hardness values, Konowalczyk recommends the highest possible case hardening depth CHD_{550} and a small difference between the surface hardness HV_S and the core hardness HV_C [1]. Accordingly, a low surface hardness HV_S with the highest possible core hardness HV_C, so that a reduction in the tensile residual stresses critical to tooth flank fracture is achieved at high material depths [1]. Witzig shows by measurements that there are limits for increasing the case hardening depth CHD_{550}, because higher strength-reducing tensile residual stresses are the consequence of a higher case hardening depth CHD_{550} [2].

Nonmetallic inclusions According to the work of Murakami, non-metallic inclusions have a considerable influence on the strength and thus on the load capacity [21]. A significant negative influence of defects located in the highly stressed tooth volume has also been documented and proven with regard to the tooth flank fracture load capacity [1–3, 13, 20]. Witzig identifies defects in a depth range of twice the case hardening depth CHD_{550} at the transition between the surface and core structure for test gears made of both 20MnCr5 and 18CrNiMo7-6 as crack initiation points [2]. Witzig further explains that it is not the inclusions themselves that lead to the type of flank fracture, but rather the high material stress present at greater material depths is decisive and the defect is identified as the damage starting point due to its stress-increasing effect [2]. Konowalczyk can always identify a defect as the crack initiation site for the tooth flank fractures that occurred in his test rig investigations, regardless of the external load, from which he concludes that the crack does not start at the location of maximum stress, but at the location of maximum exposure [1]. Furthermore, the defect size has a stronger influence on the load capacity at low hardnesses [1]. Goergen developed an analogy test rig to investigate the damage type tooth flank fracture and came to the conclusion that a defect in the volume must be present for crack initiation [7, 8].

2.2.2 Influencing geometry factors

In the literature, a significant influence of the gear geometry on the tooth flank fracture load capacity is found across the board. Influences on the tooth flank fracture load capacity are seen in the macro geometric gear parameters normal pressure angle α_n, helix angle β, normal modulus m_n, normal tooth thickness s_n and the profile shift x. Tobie does not rule out a significant influence of the macro geometry on the basis of experimental load capacity tests [4]. Regarding the geometries tested, he refers to a low normal module m_n in relation to the center distance a and a low tooth tip height in relation to the pitch circle [4]. As a result of these properties the ratio of case-hardened surface layer to the residual stress cross-section of the core in the damage-relevant area is correspondingly high [4]. A high normal pressure angle is classified in various studies as reducing the tooth flank fracture load capacity [2, 8, 9, 20, 22, 23]. In a calculation study, Beermann et al. found a clear trend towards higher safety against tooth flank fracture with a lower normal pressure angle α_n [22]. In test bench studies, Witzig found a higher bearable torque without damage due to flank fracture at a lower normal pressure angle α_n [2]. The positive influence of a low normal pressure angle α_n is justified by the associated reduction in the equivalent radius of curvature ρ and the smaller Hertzian contact width b_H [2]. With a smaller equivalent radius of curvature the depth of the occurring stress maximum is closer to the surface, where the case hardening results in a higher material strength [2]. Goergen confirms the influence in a sensitivity analysis with the FE-based flank fracture calculation based on the work of Konowalczyk [1, 8]. Goergen's calculations show a drop in the endurance flank pressure σ_{DF} with increasing pressure angle and an almost constant endurance torque M_{DF} [8]. He attributes this to larger stressed volumes below the Hertzian contact width [8]. As a result, large areas of the tooth volume are highly stressed and high stresses are extended to higher depths, although the maximum flank pressure decreases. Goergen recommends the transverse pressure angle α_{wt} as a suitable parameter instead of the normal pressure angle α_n, as even with low normal pressure angles α_n, high transverse pressure angles α_{wt} can be present with a high profile shift sum Σx [8]. He states that neither very high transverse pressure angles ($\alpha_{wt} > 21°$) nor very low transverse pressure angles ($\alpha_{wt} < 19°$) are beneficial in terms of tooth flank fracture load capacity [8]. He explains, that in both cases one of the stress mechanisms (primary stress due to Hertzian contact or secondary stress due to bending and transverse shearing) is increased, which reduces the tooth flank fracture load capacity [8].

With regard to the profile shift x, the majority of research results indicate a positive influence of high profile shifts x and thus high normal tooth thicknesses s_n [8, 17]. MackAldener et al. and Al et al. demonstrate the positive influence of "non-slender" teeth [16, 17]. As part of a semi-analytical method, the influence of geometry and material parameters on the risk of TIFF damages is investigated using three tooth geometries that differ primarily in terms of slenderness, i.e. non-slender, original and slender [10, 11]. MackAldener et al. carry out a parameter study with the parameters fatigue strength σ_{crit}, fatigue sensitivity of the material to normal stresses a_{cp}, tooth slenderness ratio S, case hardening depth CHD_{550} and the normal force F_N on the tooth flank. The slenderness ratio S is calculated as the ratio of the active tooth height to the tooth thickness [10]. As a result of the parameter study, MackAldener et al. obtained the correlation between the above-mentioned parameters and the CIRF factor. In descending order, the influence of the parameters on the CIRF factor is as follows: Fatigue strength σ_{crit}, slenderness ratio S, tooth load (applied torque T), fatigue sensitivity of the material to normal stresses a_{cp} and case hardening depth CHD_{550}. The parameter study documents that the risk of TIFF increases as the fatigue strength σ_{crit} decreases and the slenderness ratio S increases [10]. Goergen also finds a positive influence of a high profile shift x on the tooth flank fracture load capacity and justifies this with reduced tensile residual stresses in the core and a higher moment of inertia in the lower half of the tooth, which reduces the stresses from bending, compression and transverse shearing [8].

According to Goergen, increasing the helix angle β leads to greater maximum contact line lengths l_{max} and total overlap ε_γ, but also to an increase in the critically stressed volume [8]. Nevertheless, Goergen summarizes an increasing fatigue strength torque M_{DF} with increasing helix angle β [8]. Beermann, on the other hand, shows a decreasing safety against tooth flank fracture and cites the increased pressure angle due to higher helix angles as a possible explanation [22].

With regard to the influence of tip shortening, Goergen found no or a negative influence on the tooth flank fracture load capacity [8]. Shortening the pinion tip d_{a1} reduces the total overlap ε_γ, on the other hand increases the tooth height in the single meshing area $h_{B\rightarrow D}$, which leads to a larger lever arm [8]. Nevertheless, calculations of Goergen show a constant endurance torque [8]. This is due to the fact that the single point of contact shifts in the direction of the pinion root, where there are increased tooth cross-sections and thus the stresses from bending and transverse shearing are lower despite the larger lever arm [8]. Shortening the tip on the mating gear d_{a2} results in the same way on the pinion in a shift of the single meshing area in the direction of the tooth tip and an increase in the tooth height in the single meshing area $h_{B\rightarrow D}$ [8]. As a result, areas with smaller tooth cross-sections are critically stressed, which leads to higher stresses due to bending and transverse shearing [8]. Goergen sees an increase in the common tooth width b as an effective measure of increasing the tooth flank fracture load capacity [8]. Although the positive effect on the tooth flank fracture load capacity is lower than for the pitting load capacity due to the simultaneously larger stressed component volumes [8].

2.3 FE-based calculation of TFF load capacity under reverse bending

The FE-based approach for calculating the tooth flank fracture load capacity is based on the work of Konowalczyk and has been modified in recent years by Goergen and extended by Rolzhäuser et al. to include the influence of the alternating bending load [1, 8, 14]. Goergen states that Konowalczyk has a deficit in the physically correct consideration of the residual stress state, as the stresses calculated in a sectional plane are squared to form equivalent stresses and the compressive and tensile components of the residual stresses cannot be differentiated as a result [1, 8]. Therefore, Goergen modified the calculation method with the shear stress intensity hypothesis adapted by Liu et al. using Eq. 1 so that normal mean stresses are considered true to the sign (Fig. 2, bottom right) [8, 24]. This is especially in the transition area between compressive residual stresses and tensile residual stresses important [8].

$$\sigma_{va}^2 + m \cdot \sigma_{vm,\tau}^2 + n \cdot \sigma_{vm,\sigma} = \sigma_W^2 \tag{1}$$

$$\sigma_{va} = \left(a \cdot \sigma_{va,\tau}^2 + b \cdot \sigma_{va,\sigma}^2\right)^{1/2} \tag{2}$$

$\sigma_{va,\tau}$	MPa	Equivalent shear stress amplitude
$\sigma_{va,\sigma}$	MPa	Equivalent normal stress amplitude
$\sigma_{vm,\tau}$	MPa	Equivalent mean shear stress
$\sigma_{vm,\sigma}$	MPa	Equivalent mean normal stress
σ_W	MPa	Fatigue limit
a	–	Material coefficients based on σ_W, σ_{Sch}, τ_W, τ_{Sch} acc. to Liu et al. [24]
b	–	
m	–	
n	–	

The equivalent shear stress amplitude $\sigma_{va,\tau}$ and the equivalent normal stress amplitude $\sigma_{va,\sigma}$ are calculated according to Eqs. 3 and 4. Based on preliminary work of Konowalczyk and Goergen, the double amplitude of the shear stress of all cutting planes is assumed to be critical for damage in this work (Eq. 3; [1, 8]). To calculate the equivalent mean stresses $\sigma_{vm,\tau}$ and $\sigma_{vm,\sigma}$, the mean shear stresses are weighted over the shear stress amplitudes (Eq. 5), and the mean nor-

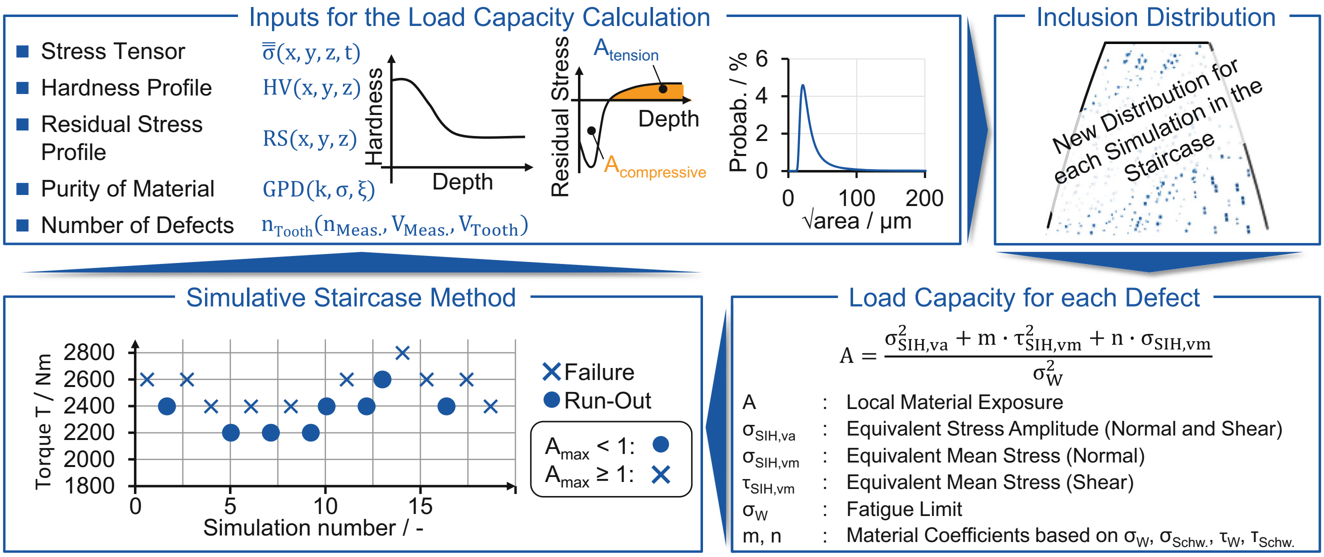

Fig. 2 Procedure of the FE-based tooth flank fracture load capacity calculation [1, 8, 14]

mal stresses over the normal stress amplitude (Eq. 6) in all cutting planes [24].

$$\sigma_{va,\tau} = \sqrt{\frac{15}{8\pi}\int\limits_{\gamma=0}^{\pi}\int\limits_{\varphi=0}^{2\pi}\tau_{\gamma\varphi,a}^{2}\sin\gamma d\varphi d\gamma} \tag{3}$$

$$\sigma_{va,\sigma} = \sqrt{\frac{15}{8\pi}\int\limits_{\gamma=0}^{\pi}\int\limits_{\varphi=0}^{2\pi}\sigma_{\gamma\varphi,a}^{2}\sin\gamma d\varphi d\gamma} \tag{4}$$

$$\sigma_{vm,\tau} = \sqrt{\frac{\int\limits_{\gamma=0}^{\pi}\int\limits_{\varphi=0}^{2\pi}\tau_{\gamma\varphi,a}^{2}\tau_{\gamma\varphi,m}^{2}\sin\gamma d\varphi d\gamma}{\int\limits_{\gamma=0}^{\pi}\int\limits_{\varphi=0}^{2\pi}\tau_{\gamma\varphi,a}^{2}\sin\gamma d\varphi d\gamma}} \tag{5}$$

$$\sigma_{vm,\sigma} = \frac{\int\limits_{\gamma=0}^{\pi}\int\limits_{\varphi=0}^{2\pi}\sigma_{\gamma\varphi,a}^{2}\sigma_{\gamma\varphi,m}\sin\gamma d\varphi d\gamma}{\int\limits_{\gamma=0}^{\pi}\int\limits_{\varphi=0}^{2\pi}\sigma_{\gamma\varphi,a}^{2}\sin\gamma d\varphi d\gamma} \tag{6}$$

For the calculation of local material exposure, the fatigue limit for internal defects σ_W is determined according to Murakami based on the local hardness HV1 and the defect size $\sqrt{\text{area}}$ using Eq. 7 [21]. The necessary strength values for alternating torsional loading τ_W, pulsating axial loading σ_{Sch}, and pulsating torsional loading τ_{Sch} are calculated with Eqs. 8, 9 and 10 according to Böhme and Liu [24, 25]. The mean stress sensitivity is calculated following Niemann et al. using Eq. 11 [26].

$$\sigma_W = \frac{HV1 + 120}{\sqrt[6]{area}} \tag{7}$$

$$\tau_W = \frac{\sigma_W}{-5 \cdot 10^{-4} \cdot HV1 + \sqrt{3}} \tag{8}$$

$$\sigma_{Sch} = \frac{2\sigma_W}{1 + M} \tag{9}$$

$$\tau_{Sch} = \frac{4\tau_W}{1 + \frac{2\sigma_W}{\sigma_{Sch}}} \tag{10}$$

$$M = 0.00035 \cdot R_M - 0.1 \tag{11}$$

σ_w	MPa	Fatigue limit for internal defects
τ_W	MPa	Strength value for alternating torsional loading
σ_{Sch}	MPa	Fatigue limit for pulsating axial loading
τ_{Sch}	MPa	Strength value for pulsating torsional loading
M	MPa	Mean stress sensitivity
R_M	MPa	Tensile strength

The calculation process of the FE-based tooth flank fracture load capacity calculation corresponds to a simulative staircase method and is shown in Fig. 2. Inputs needed for calculation are the stress tensor time sequence, the hardening depth profile, the residual stress depth profile and information about material purity, see Fig. 2, top left. Based on the selected distribution function for the inclusions, the tooth volume to be calculated, and the determined inclusion density per cubic millimeter, inclusions of varying sizes are randomly distributed throughout the tooth volume. In the next step, local exposure is calculated at each defect scattered within the tooth volume. If there is at least one defect where an exposure $A \geq 1$ is calculated, this virtual test is evaluated as a failure, and the next test is conducted with a torque T reduced by one increment. Conversely, if just exposures $A < 1$ occur for every defect, the test is considered a run-out, and the subsequent test is simulated with a torque T increased by one increment. In this manner, a virtual staircase is progressively simulated from which the endurance torque $M_{50\%}$ for a failure probability $P_A = 50\%$ and the standard deviation are determined using Hück's method [1, 8, 27].

The approach for calculating the tooth flank fracture load capacity was applied in preliminary work to the spur gear test variant "B00" from the FVA research project no. 718 I ("Local alternating bending load capacity") [14, 28]. From the endurance torque $M_{DF,50\%,}$ which is defined for a failure probability of $P_A = 50\%$, a tooth flank fracture load capacity reduction at $R_M = -1$ was observed for the test pinion "B00" in a simulation study when comparing the two load types purely pulsating and purely alternating. The alternating bending load therefore results in a reduction in load capacity for the gear geometry tested. A comparison of the results from FVA research project no. 718 shows that the reduction in load capacity due to the alternating bending load is lower for the tooth flank fracture load capacity than for the tooth root load capacity. This is explained by the higher stress amplitudes present in the tooth root. Furthermore, when looking at the fractures in the face section, it is found that the fracture-initiating defects are all located in the loaded right half of the tooth under purely pulsating load, whereas they are distributed throughout the entire tooth volume under alternating bending load. In addition, the fracture-initiating defects at $R_M = -1$ are located more centrally in the tooth volume in the tooth thickness direction or at higher depths than at $R_M = 0$. The cause is seen in the superposition of the stresses centrally in the tooth thickness direction with alternating bending load. Consequently, this results in a locally higher stress amplitude compared to purely pulsating loads. At $R_M = -1$, the fracture-initiating defects shift towards higher material depths, as the stress there is increased due to higher stress amplitudes compared to $R_M = 0$. Accordingly, the hypothesis is derived that under alternating bending loads the demands on the material purity are higher at a constant load level, as a larger volume is subjected to high stresses.

3 Objective and approach

As a result of the continuous optimizations of recent years, sub-surface-induced gear damages are becoming increasingly relevant for gear design. To this end, the development and influencing factors of tooth flank fractures and internal tooth fatigue fractures caused by defects were discussed as part of the review of the state of the art. While the influence of the alternating bending load with regard to the tooth root load capacity has already been investigated and anchored in the standard design, only a few findings from research work are available with regard to the tooth flank fracture load capacity. Earlier work by MackAldener indicates a considerable influence [10–12, 16]. Preliminary work also identified a load capacity-reducing influence [14]. Further research on this subject necessitates additional simulation studies to investigate the influence of alternating load. The objective of this work is thus derived as follows:

Design of a tooth flank fracture-critical test gear set under reverse bending load To achieve the objective, the preliminary work carried out is used as a basis [14]. In the first step, an extended influence analysis is carried out. While the focus in the preliminary work was on the endurance torque resulting from the stair-case method and the position of the fracture-initiating inclusions, the focus in this work is the exposure depth curve, the stressed volume and the use of different equivalent stress hypotheses. Subsequently, the influence of macro geometric changes on the exposure depth curve is investigated. Based on the investigation of the influence of macro geometry, a gear geometry is designed that reacts with a high sensitivity with regard to the tooth flank fracture load capacity when an alternating bending load is applied. Finally, the robustness of the design against changes in the hardening depth and residual stress depth profile is calculated.

4 Extended analysis of influence of reverse bending on TFF load capacity

In the following sections, an extended influence analysis is carried out based on the preliminary work [14]. To this end, the gear geometry under consideration is presented first. The geometry is then examined with regard to the material stress for various equivalent stress hypotheses.

4.1 Reference gear geometry and boundary conditions

The gear geometry, to which the extended calculation approach is applied, is the spur gear test variant "B00" from the FVA research project No. 718 I ("Local alternating load capacity") [28]. The gear set has a normal module of $m_n = 2$ mm, was slightly corrected micro geometrically and is made of the material 16MnCr5, see Fig. 3 left. For modeling of the hardness depth curve of the test pinion the Lang approach is used [29]. This approach is able to reproduce the measurements in comparison with the hardness measurements from FVA 718-I [28, 30]. The test pinion has a case hardening depth of $CHD_{550} = 0.4$ mm. The residual stress depth curve is determined according to the approach of Iss et al. and considers tensile residual stresses in the

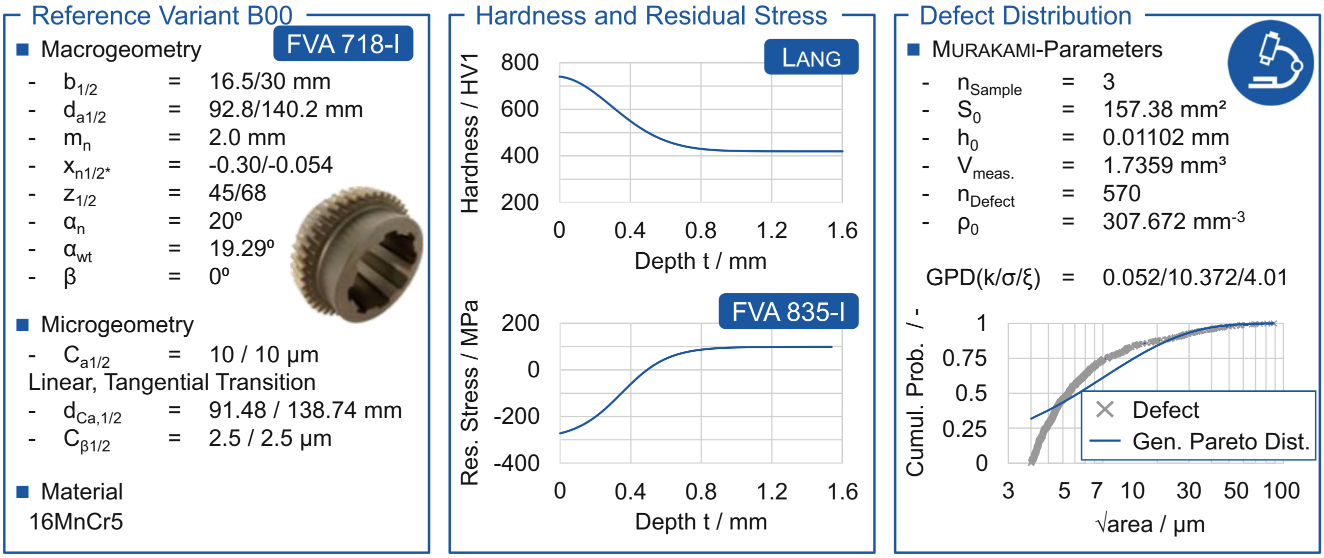

Fig. 3 Gear geometry and material properties [14, 28]

core, see Fig. 3 center [5]. To determine the distribution of defects, microsection analyses were carried out on embedded samples of a test pinion. For the basic procedure, refer to Brecher et al. [31]. The cumulative probability of the detected defects is shown in Fig. 3 over the logarithmically plotted Murakami-parameter $\sqrt{\text{area}}$ and is approximated with the General Pareto Distribution (GPD) for the flank fracture calculation, as this represents a good approximation, particularly in the area of larger defects relevant for the load capacity calculation. The material properties of the gears are kept constant in the subsequent macro geometry variation investigations. After the macro geometric design has been carried out, the robustness of the design against variations in hardening depth and residual stress depth are examined in more detail.

4.2 Influence of used stress hypothesis

In preliminary work, the influence of the alternating load on the fatigue strength and the position of the crack-initiating defects were determined, see 2.3 [14]. It should be noted that the selected equivalent stress hypothesis is expected to have a considerable influence on the resulting reduction in load capacity under bidirectional loading [14]. Therefore, the reference geometry “B00” is examined and evaluated below with various equivalent stress hypotheses, which are used in common calculation methods for tooth flank fracture load capacity calculation. Using the FE-based tooth flank fracture calculation according to Sect. 2.3, the exposure depth curves for the hypotheses according to Simbürger, Zenner/Liu, Dang Van, Weber and Findley are calculated and compared for unidirectional and bidirectional loading [16, 24, 32–35]. The selected load level is $M = 550\,\text{Nm}$ in the range of the short time fatigue. The evaluation of the exposure depth curves is centered in the tooth width direction ($z = 0\,\text{mm}$) on a diameter of $d_{\text{Eval.}} = 88.4\,\text{mm}$ projected onto the tooth flank at the level of the lower single contact area, where the crack-initiating inclusions for both unidirectional and bidirectional loading were calculated in preliminary work [14]. Since the non-metallic inclusions are randomly present in the volume, a constant defect size with a Murakami-parameter of $\sqrt{\text{area}} = 90\,\mu\text{m}$ is assumed for the calculation of the exposure depth curves for the purpose of comparability.

The calculated exposure depth curves are shown in Fig. 4 for the various equivalent stress hypotheses. The blue exposure depth curve represents the unidirectional load case, while the yellow curve shows a bidirectional load (meshing of left and right flank). Since the applied torque ratio for bidirectional loading in the context of this work is $R_M = -1$ and the tooth contour is symmetrical, the evaluation of the exposure depth curves in one half of the tooth thickness is sufficient.

Using Simbürger’s hypothesis, there is only a slight difference in the exposure between unidirectional and bidirectional loading. Only at greater depths does bidirectional loading result in $\Delta A = 6.8\%$ higher exposure. In contrast, the calculated exposure depth curve according to Zenner/Liu hypotheses shows clearer differences. The yellow curve for bidirectional loading reaches its maximum at a slightly greater depth and at a depth of $t = 1.4\,\text{mm}$ there is an approximately $\Delta A = 32\%$ higher exposure with bidirectional loading. When using the equivalent stress hypothesis according to Dang Van, there is no difference between the blue and yellow exposure depth curves (curves are congruent). Therefore, using this hypothesis, no reduction in load capacity is to be expected in the simulation of the stair-case method. The reason for this is that Dang Van

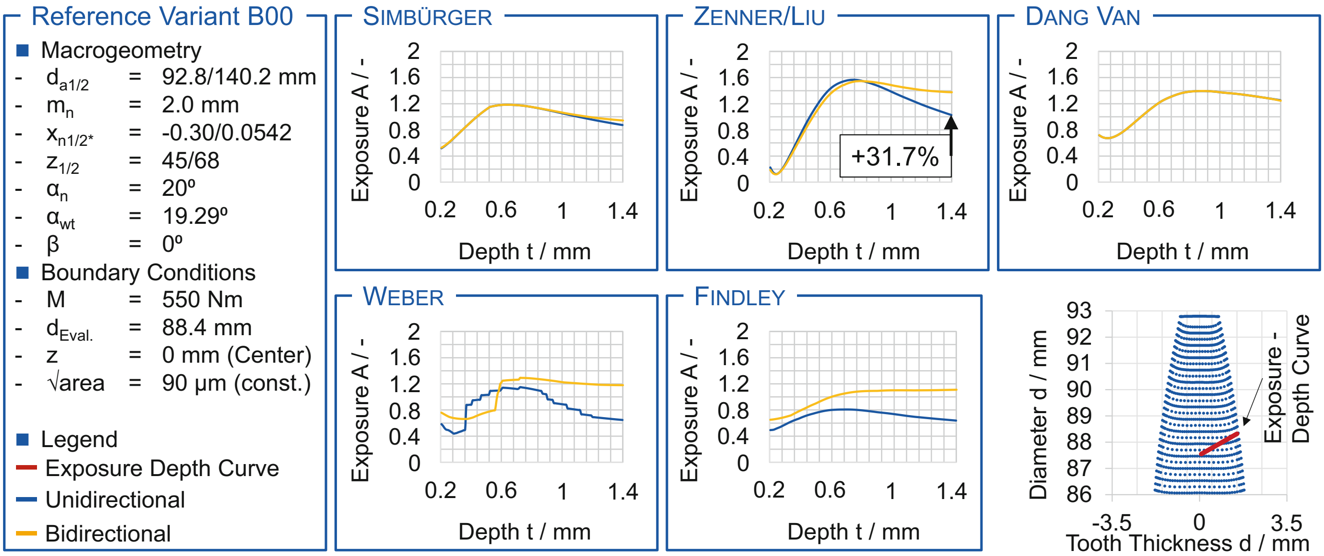

Fig. 4 Exposure depth curve for different stress hypotheses

does not evaluate the rolling contact with amplitudes and averaging, but uses the maximum main shear stress at one point in time [8, 32]. The critical plane equivalent stress hypotheses according to Weber provides higher exposures for bidirectional loading from a depth of t = 0.6 mm. While the depth curve for unidirectional loading decreases again towards higher depths, the bidirectional curve remains approximately constant at high exposure values after reaching its maximum. The same can be observed with the exposure depth curves calculated according to Findley's stress hypothesis. The curve for bidirectional loading is above the one for unidirectional loading at every depth. While the blue curve drops again after reaching a maximum exposure at a depth of t = 0.6 mm, the bidirectional (yellow) curve is almost constant from a similar depth.

The Simbürger approach is used in the work of Witzig and Wickborn and forms the basis of ISO/TS 6336-4 (2019) [2, 3, 30]. The Zenner/Liu approach is used by Goergen [8]. In the state of the art on the influence of the alternating bending load on the tooth flank fracture load capacity, the work of MackAldener, who uses the Findley hypothesis, is particularly noteworthy [10–12, 16, 33]. Therefore, for these three approaches, the exposure distribution in the normal section is examined in more detail below and the highly stressed volume is compared. The highly stressed volume is defined according to Eq. 11 as the ratio of the number of nodes with an exposure equal to or greater than 90% of the maximum exposure to the total number of nodes.

$$\mathrm{HSV}_{90} = \frac{\mathrm{n_{Nodes}}\ \text{with} \geq 90\% \cdot A_{max}}{\mathrm{n_{Nodes}}} \qquad (12)$$

HSV_{90}	–	Highly stressed volume (90%)
$\mathrm{n_{Nodes}}$	–	Number of nodes
$\mathrm{A_{max}}$	–	Maximum exposure

Figure 5 shows the plotted exposures in the normal section for the hypotheses according to Simbürger, Zenner/Liu and Findley for unidirectional and bidirectional loading. Since the helix angle is $\beta = 0°$, it can be assumed that the exposures in the cross-section are constant over the tooth width. Furthermore, the ratio of the highly stressed volume for bidirectional loading $\mathrm{HSV}_{90,\mathrm{bi}}$ to the highly stresses volume for unidirectional loading $\mathrm{HSV}_{90,\mathrm{uni}}$ is calculated. In the exposure plot for the Simbürger approach, little changes are observed for bidirectional loading compared to unidirectional loading. The bidirectional plot is almost the mirror image of the unidirectional plot. In the exposure plot for the Zenner/Liu approach, on the other hand, the volume in the area of the symmetry line of the tooth is also highly stresses due to the applied alternating bending load, which is not observed in the case of unidirectional loading. In the case of bidirectional loading, a highly stresses volume that is $\mathrm{QHSV}_{90} = 1.63$-times greater is calculated. For the Findley case, it should first be noted that the exposure level with unidirectional loading is significantly lower than with Simbürger and Zenner/Liu. In the case of bidirectional loading, the level of exposure with Findley increases in both halves of the tooth. There is also a high exposure around the symmetry line of the tooth, like in calculation with Zenner/Liu. Overall, bidirectional loading results in a $\mathrm{QHSV}_{90} = 4.43$-times greater highly stressed volume.

In order to determine the equivalent stress hypothesis to be used for the macro-geometry variation, or the design of a test gear set within the scope of this work, the effect

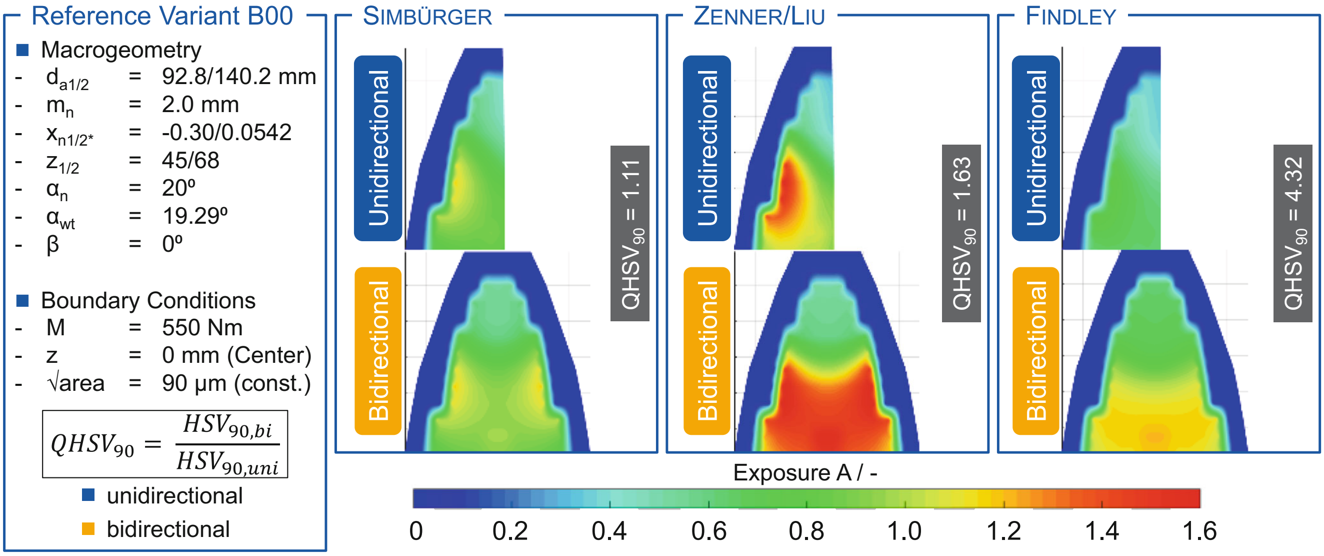

Fig. 5 Exposures in normal section for selected stress hypotheses

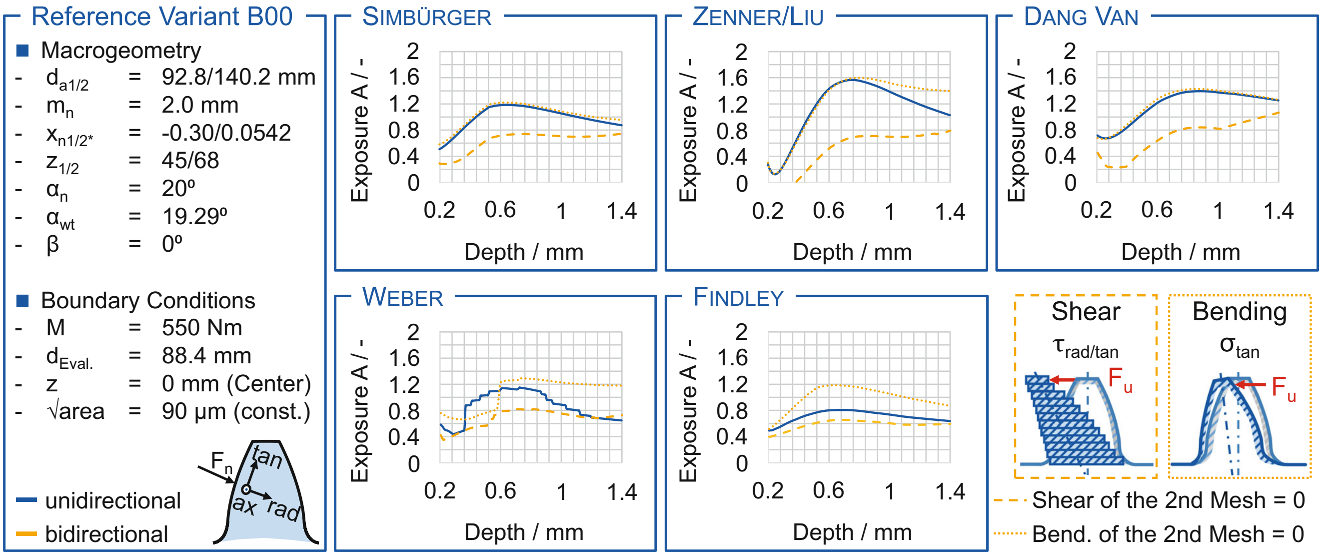

Fig. 6 Manipulation of tensor components of the second mesh

of the shear component $\tau_{rad/tan}$ and the tension/compression component σ_{tan} is investigated for the various hypotheses. According to the hypotheses described in Sect. 2.3 the stress tensor time sequence for the meshing of the two flanks is connected in time direction when considering bidirectional loading. In order to investigate the effect of individual components on the stress depth curve, the time curve is manipulated in such a way that the stress component under consideration is set to zero for the rolling of the second mesh. The procedure is subject to the basic expectation that the exposure increases with bidirectional loading. However, since an amplitude and mean stress value is considered, the exposure does not necessarily have to increase. Therefore, if one of the considered stress components of the second mesh has a strong influence, the manipulated bidirectional mesh deviates significantly from that of unidirectional loading. The results of the investigation are shown in Fig. 6. The dashed yellow curve shows the exposure depth curve in which the shear component $\tau_{rad/tan}$ was set to zero. For all five hypotheses, the dashed curve decreases, meaning that this component has an influence. The biggest difference is seen with Zenner/Liu. The dotted yellow curve shows the exposure depth curve in which the tangential component σ_{tan} was set to zero. This shows a smaller overall influence, i.e. a smaller deviation from the unidirectional blue curve than the dashed curves. A reduction in load capacity with alternating bending load is therefore more likely to be due to the opposing shearing of the second mesh than to the tangential tension/compression component.

4.3 Intermediate conclusion and evaluation

The calculation of the exposure depth curves has shown that the influence of the alternating bending load on the tooth flank fracture load capacity can be modeled with the FE-based tooth flank fracture calculation. When different equivalent stress hypotheses are used, there are clear differences in the exposure depth curves. The hypothesis according to Dang Van shows no differences in the exposure depth curve with bidirectional calculation and is therefore not suitable. Although the hypotheses according to Weber and Findley show significant increases in exposure with bidirectional calculation, they deliver load capacities that are clearly too high or very low exposures, which Goergen also shows in validation calculations [8]. The hypothesis according to Zenner/Liu provides results which, compared to the use of the hypothesis according to Simbürger, are closer to the state of the art. Therefore, the hypothesis according to Zenner/Liu is used in the following, as Goergen also suggests in his work [8].

5 Design of testing gear set

After the reference geometry “B00” was examined in more detail in the previous section, the reference geometry is modified macro geometrically in the following chapters. The aim is to show tendencies that make a gear design as sensitive as possible regarding the risk of tooth flank fracture under alternating bending load.

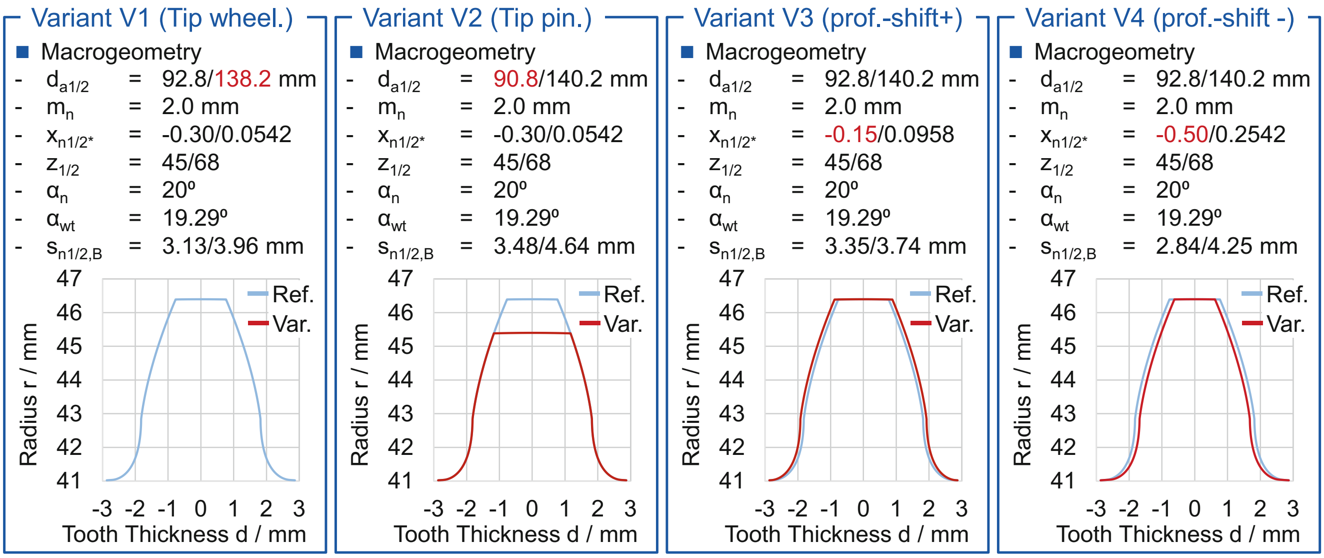

Fig. 7 Variation of the macro geometry—overview of variants and pinion tooth contour

5.1 Variation of macro geometry

Goergen describes tip shortening on the pinion and mating gear as modifications that increase the risk of tooth flank fracture [8]. The state of the art also indicates that slender teeth in particular are subject to an increased risk of tooth flank fractures or internal tooth fatigue fractures [11, 17]. The focus of macro geometry variation is therefore on shortening the tip and adapting the tooth height to thickness ratio. Figure 7 shows the different geometries that are calculated as part of the geometry variation as well as the tooth contour of the pinion compared to the reference contour.

The reference variant "B00" of the pinion is shown in blue and the modified variant in red. For variant V1, the tip diameter of the counter wheel was shortened by two millimeters to $d_{a2} = 138.2\,\mathrm{mm}$. The geometry of the pinion therefore still corresponds to the reference geometry B00. With variant V2, on the other hand, the tip diameter of the pinion is shortened by two millimeters to $d_{a1} = 90.8\,\mathrm{mm}$. Variants V3 and V4 are used to explicitly investigate the influence of the tooth height to thickness ratio. For this purpose, the tool profile shift x_1 of the pinion is increased to $x_{1*} = -0.15$ for variant V3. This increases the normal tooth thickness $s_{n1,B}$ of the finished tooth at the lower single contact area of the pinion by 7% to $s_{n1} = 3.35\,\mathrm{mm}$. In variant V4, the tooth height to thickness ratio of the tooth is increased by reducing the tool profile shift x_{1*} of the pinion to $x_{1*} = -0.50$. Accordingly, the normal tooth thickness at the lower single contact area is reduced by 9% to $s_{n1,B} = 2.84\,\mathrm{mm}$.

Once the variants have been defined, the exposure depth curve for unidirectional and bidirectional loading is calculated and compared with each other. The boundary conditions are selected identical to Sect. 4.2. The selected load level is $M = 550\,\mathrm{Nm}$ in the area of the short time fatigue. The exposure depth curves are evaluated in a central position in tooth width direction ($z = 0\,\mathrm{mm}$) on a diameter of $d_{\mathrm{Eval.}} = 88.4\,\mathrm{mm}$ projected onto the tooth flank at the level of the lower single contact area with a constant Murakami parameter of $\sqrt{\mathrm{area}} = 90\,\mu\mathrm{m}$. The results of the variant calculation are shown in Fig. 8. Particular attention is paid to the difference in the exposure depth curve at high material depths. For all variants, it can be observed that the maximum exposures are reached from a depth of $t = 0.75\,\mathrm{mm}$. This corresponds to the selected boundary conditions in Fig. 3 meaning the transition to core hardness in the hardening depth curve and the depth range where tensile residual stresses that reduce load capacity are already acting.

With variant V1 (tip shortening counter wheel), it is noticeable that the maximum exposure is greater with bidirectional loading than with unidirectional loading and is reached at slightly greater depths. The yellow exposure depth curve does not drop as much towards greater depths as the blue (unidirectional) curve, so that the difference between the two curves increases towards greater depths. At a depth of $t = 1.4\,\mathrm{mm}$ around the symmetry line of the tooth, bidirectional loading results in $\Delta A = 46\%$ higher exposure than unidirectional loading (Fig. 8, left). For variant V2 (tip shortening pinion), an almost identical stress depth curve for unidirectional and bidirectional loading can be seen up to a depth of $t = 0.9\,\mathrm{mm}$. Towards greater depths, the bidirectional curve drops less sharp, so that at a depth of $t = 1.4\,\mathrm{mm}$, a $\Delta A = 36\%$ higher exposure results for bidirectional loading. For variant V3 (increased tool profile shift), it should first be noted that the maximum exposure is lower than for all other variants. A greater tooth thickness is therefore beneficial to the tooth flank fracture load capacity for

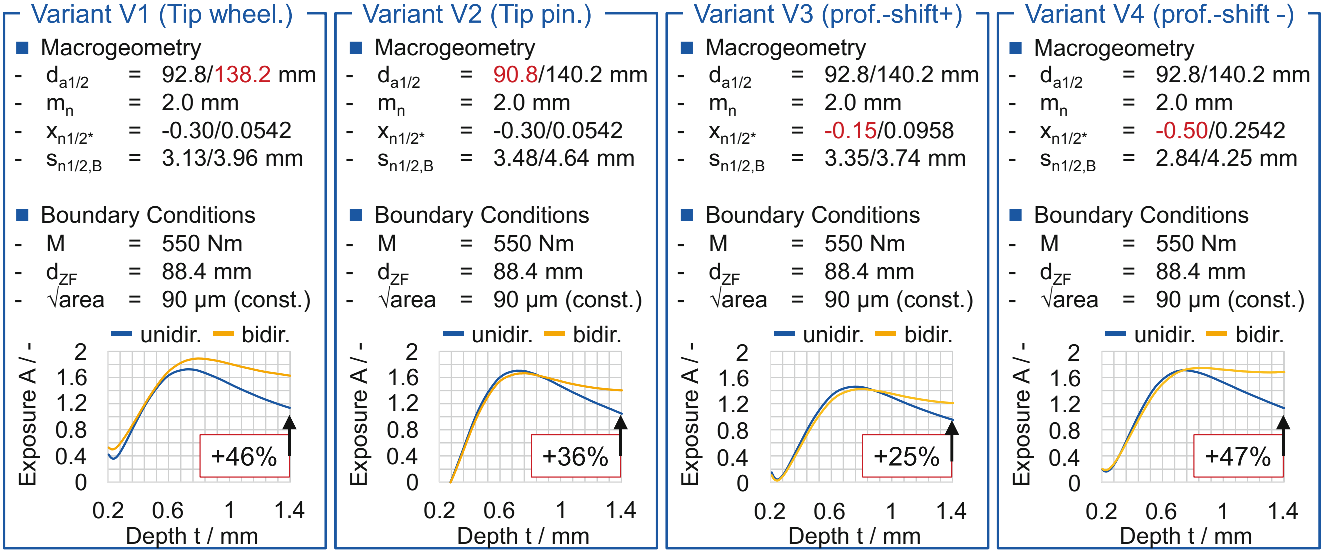

Fig. 8 Variation of the macro geometry—Comparison of exposure depth curves

both unidirectional and bidirectional loading. At a depth of t = 1.4 mm, variant V3 results in the smallest difference in exposure between unidirectional and bidirectional loading of ΔA = 25%. With variant V4 (reduced tool profile shift), almost identical exposure depth curves can be observed up to a depth of t = 0.75 mm. Subsequently, the bidirectional curve is almost constant with significantly higher exposure than the unidirectional curve, which drops significantly after reaching its maximum at t = 0.72 mm (Fig. 8, right). At t = 1.4 mm, this results in a ΔA = 47% higher exposure for bidirectional loading compared to unidirectional loading. Although the amount of total overlap ε_γ of the reference variant B00 and variant V4 are identical, variant V4 reacts significantly more sensitively to the alternating bending load. With variants V3 and V4 in particular, the influence of slender teeth on the tooth flank fracture load capacity in general and a clear influence on the tooth flank fracture load capacity under alternating bending load in accordance with the state of the art can therefore be confirmed (Sect. 2.2).

Based on the results of the macro geometry variation, a further variant V5 is designed, which combines the modifications of variants V1 and V4. In variant V5, the tip of the mating gear is shortened to $d_{a2} = 138.2$ mm and the tool profile shift x_{1*} on the pinion is reduced to $x_{1*} = -0.50$. Figure 9 shows the results of the tooth flank fracture calculation of variant V5 compared to reference variant B00.

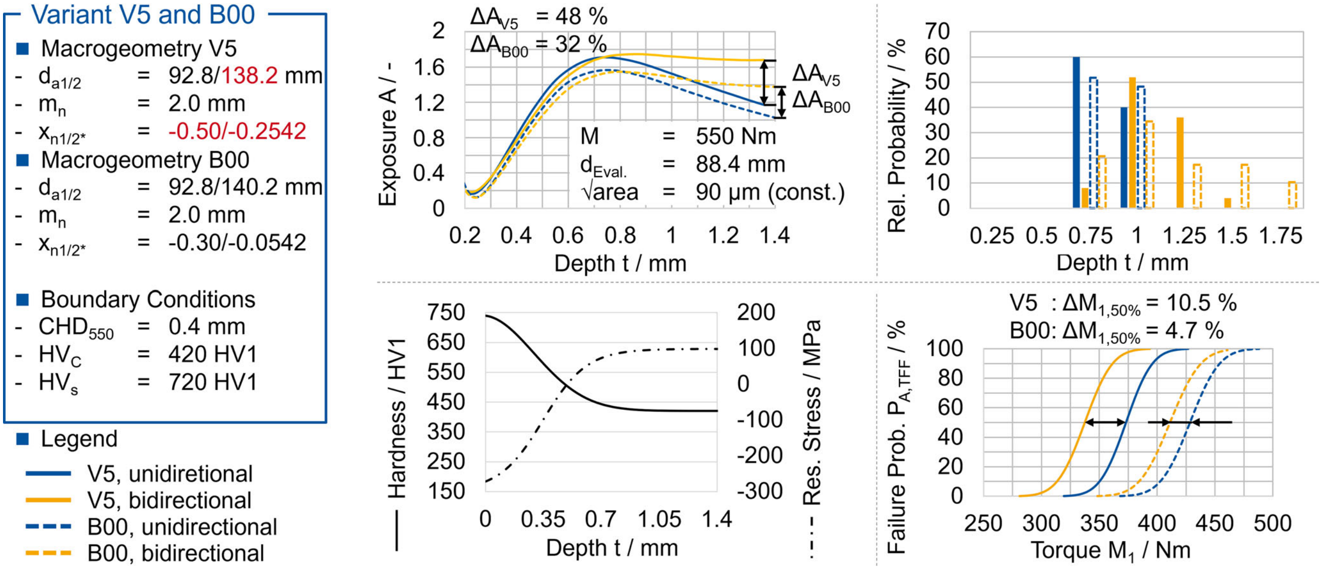

Fig. 9 Influence of Macro geometry—Evaluation of variant V5

The macro geometric adjustments result in a lower normal tooth thickness at the lower single contact area $s_{n1,B}$ and a higher tooth height in the single contact area. If the exposure depth curves are compared for constant boundary conditions at a torque of $M = 550\,\text{Nm}$ and Murakami parameter $\sqrt{\text{area}} = 90\,\mu\text{m}$ on an evaluation diameter of $d_{\text{Eval.}} = 88.4\,\text{mm}$, variant V5 shows $\Delta A_{V5} = 48\%$ higher exposure under bidirectional loading. In contrast, the reference variant B00 only shows a $\Delta A_{B00} = 32\%$ higher exposure in the area of the symmetry line of the tooth. With regard to the depth distribution of the crack-initiating defects, a shift in crack initiation towards higher depths can be observed for both variants V5 and B00, whereby it should be noted here that the normal tooth thickness s_n of the two variants is no longer identical (Fig. 9, top right). The increased exposure of variant V5 is also reflected in the endurance torque $M_{1,50\%}$ for a 50-percent failure probability. The reduction in load capacity due to the applied alternating bending load was increased to $\Delta M_{1,50\%} = 10.5\%$ for variant V5 compared to the reference variant (Fig. 9, bottom right). As the boundary conditions regarding hardness, residual stresses and distribution of defects were assumed to be the same for the calculation of both variants, the differences are solely due to the macro geometric adjustments. This shows that different geometries react with different sensitivity to bidirectional loading. The criticality of a high tooth height to thickness ratio in particular, as described in the state of the art, with regard to the damage types of tooth flank fracture and internal tooth fatigue fracture is thus confirmed.

5.2 Sensitivity of hardness and residual stresses

To investigate the robustness of the designed variant V5 against changes in the hardness and residual stress depth profile, a further tooth flank fracture calculation with a reduced case hardening depth of $CHD_{550} = 0.3\,\text{mm}$ is carried out. The results of the calculation can be compared with the initial boundary conditions (see Sects. 4.1 and 5.1) in Fig. 10. Corresponding to the residual stress approach according to Iss et al., a reduced case hardening depth CHD_{550} also results in lower maximum amounts of tensile residual stresses in the core hardness range (Fig. 10, bottom left) [5]. The probability of failure derived from the simulated stair-case (Fig. 10, bottom right) shows that a higher case hardening depth is generally beneficial for the tooth flank fracture load capacity. However, the reduction in load capacity is greater with a higher case hardening depth. A case hardening depth of $CHD_{550} = 0.3\,\text{mm}$ results in a reduction of $\Delta M_{1,50\%,\ 0.3\,\text{mm}} = 6.5\%$. With a case hardening depth of $CHD_{550} = 0.4\,\text{mm}$, on the other hand, the reduction in load capacity is $\Delta M_{1,50\%,\ 0.4\,\text{mm}} = 10.5\%$. This effect is due to the higher tensile residual stresses at higher case hardening depths. Regarding the depth distribution of the crack-initiating defects, a shift towards higher material depths can be observed for both case hardening depths, as already observed in the previous section. Based on the position of the crack-initiating defects, the exposure depth curve was calculated for a torque of $M = 385\,\text{Nm}$ with a constant Murakami-parameter $\sqrt{\text{area}} = 90\,\mu\text{m}$ on a flank diameter of $d_{\text{Eval.}} = 89.2\,\text{mm}$ (Fig. 10, top left). For the higher case hardening depth, the maximum exposure shifts towards higher depths.

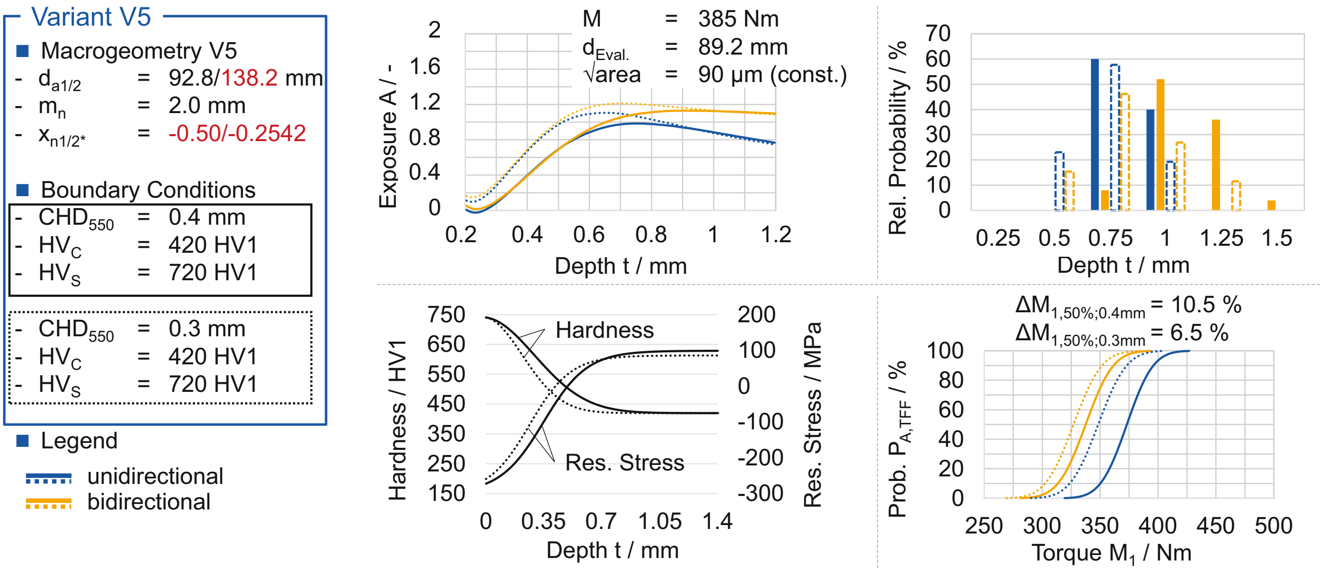

Fig. 10 Sensitivity of hardness and residual stresses of geometry variant V5

6 Summary and outlook

As a result of the constant increase in the power density of gearboxes, new types of damages are increasingly coming to the fore in gear design. Thus, tooth flank fractures and tooth interior fatigue fractures are increasingly occurring, which have their crack origin in the tooth volume below the hardened surface layer. The FE-based approach for calculating the tooth flank fracture load capacity was therefore extended to include the influence of the alternating bending load. In an initial analysis, the load capacity-reducing influence of the alternating bending load on the tooth flank fracture load capacity was simulated. Extending to this, a more in-depth analysis was carried out in the present study regarding the influence of the selected equivalent stress hypothesis and the influence of the macro geometry. It was shown that the use of the equivalent stress hypothesis according to Zenner/Liu provides meaningful results. To design a test gear geometry, a variation calculation for different macro geometries was carried out and the exposure depth curves for unidirectional and bidirectional loading were compared. It was found that the transverse shearing is particularly relevant for the reduction in tooth flank fracture load capacity under alternating bending load. Thus, the tooth height to thickness ratio can be considered to have an influence on the reduction in load capacity due to alternating bending loads. The higher the case hardening depth is selected, the greater the drop in tooth flank fracture load capacity. Determining the case hardening depth of a gear therefore requires knowledge of the macro geometric influence of the alternating bending load on the tooth flank fracture load capacity. Conversely, in order to avoid flank fractures in practical applications, large tooth thicknesses are to be preferred.

The present work represents a first step towards the design of a test gear geometry for investigating the tooth flank fracture load capacity under alternating bending loads. In future work, the design must be finalized regarding the micro geometry modifications based on further sensitivity analysis. For this purpose, the design should be also calculated and evaluated regarding its sensitivity with further residual stress approaches. Furthermore, an experimental validation must be carried out on a test bench to validate the calculation approach for alternating bending in general and the design in particular.

Funding Open Access funding enabled and organized by Projekt DEAL.

Conflict of interest J. Rolzhäuser, D. Mevissen and C. Brecher declare that they have no competing interests.

References

1. Konowalczyk P (2018) „Grübchen- und Zahnflankenbruchtragfähigkeit großmoduliger Stirnräder: Einfluss von Werkstoffreinheitsgrad, Härte- und Eigenspannungstiefenverlauf,“ Diss., Werkzeugmaschinenlabor (WZL) der RWTH Aachen. RWTH Aachen, Aachen
2. Witzig J (2012) „Flankenbruch – eine Grenze der Zahnradtragfähigkeit in der Werkstofftiefe,“ Diss., Forschungsstelle für Zahnräder und Getriebebau (FZG) der TU München. TU München, München
3. Wickborn C (2017) „Erweiterung der Flankentragfähigkeitsberechnung von Stirnrädern in der Werkstofftiefe – Einfluss von Werkstoffeigenschaften und Werkstoffdefekten,“ Diss., Forschungsstelle für Zahnräder und Getriebebau (FZG) der TU München. TU München, München
4. Tobie T (2001) „Zur Grübchen- und Zahnfusstragfähigkeit einsatzgehärteter Zahnräder: Einflüsse aus Einsatzhärtungstiefe, Wärmebehandlung und Fertigung bei unterschiedlicher Baugröße,“ Diss., Forschungsstelle für Zahnräder und Getriebebau (FZG) der TU München. TU München, München
5. Iss V, Müller D, Haupt N (eds) (2022) Eigenspannungsverläufe Flankenbruch: Abschlussbericht zum Forschungsvorhaben FVA 835 I, FVA (Forschungsvereinigung Antriebstechnik e. V.), Frankfurt a.M
6. Müller D, Tobie T, Stahl K (2023) Enhanced calculation method for tooth flank fracture risk with consideration of tensile residual stresses in larger material depths. Gear Technol 40(7):58–71
7. Goergen F, Rolzhäuser J, Mevissen D, Brecher C (2023) Analogy test rig for the generation of tooth flank fractures at large gears (WZL-double pulsator)—commissioning and first test results. Forsch Ingenieurwes 87:1–10
8. Goergen F (2023) „Analogieversuch zur Erzeugung von Zahnflankenbrüchen an Stirnrädern,“ Dissertation, Werkzeugmaschinenlabor (WZL) der RWTH Aachen. RWTH Aachen, Aachen
9. Goergen F, Brecher C, Löpenhaus C (2019) Abbildung der Zahnflankenbeanspruchung durch ein Analogiekonzept zur Erzeugung der Schadensart Zahnflankenbruch. Forsch Ingenieurwes 83(3):589–601
10. MackAldener M, Olsson M (2000) Design against tooth interior fatigue fracture, pp 18–24
11. MackAldener M (2001) “Tooth Interior Fatigue Fracture & Robustness of Gears,” Diss. KTH Stockholm, Stockholm
12. MackAldener M, Olsson M (2002) Analysis of crack propagation during tooth interior fatigue fracture. Eng Fract Mech (69):2147–2162
13. Meis J-A (2019) Flank fracture assessment of planet gears. Conf Wind Power Drives 03:1–12
14. Rolzhäuser J, Mevissen D, Brecher C (2024) Influence of reverse loading on the tooth flank fracture load capacity. AGMA Fall Tech Meeting 2024

15. Klocke F, Brecher C (2017) Zahnrad- und Getriebetechnik: Auslegung – Herstellung – Untersuchung – Simulation, 1st edn. Hanser, München
16. MackAldener M (2001) Tooth interior fatigue fracture—computational and material aspects. Int J Fatigue 23(4):329–340
17. Al B, Langlois P (2016) Analysis of tooth interior fatigue fracture using boundary conditions from an efficient and accurate LTCA. Gear Solutions: 33–39
18. Müller M, Tobie T, Stahl K (2021) Tooth flank fracture—design process for a new test gearing and first test results. AGMA Fall Tech Meeting 2021
19. Octrue M, Ghribi D, Sainsot P (2018) A Contribution to study The Tooth Flank Fracture (TFF) In cylindrical gears. Procedia Eng (213):215–226
20. Bruckmeier S (2006) „Flankenbruch bei Stirnradgetrieben," Diss., Forschungsstelle für Zahnräder und Getriebebau (FZG) der TU München. TU München, München
21. Murakami Y (2019) Metal fatigue: effects of small defects and nonmetallic inclusions, 2nd edn. Elsevier Ltd, London.
22. Beermann S (2015) "tooth flank fracture—influence of macro and micro geometry," AGMA fall technical meeting. American Gear Manufacturers Association, Alexandria
23. Beermann S, Kissling U (2015) Tooth flank fracture—a critical failure mode: influence of macro and micro geometry, KISSsoft user conference. India, pp 1–14
24. Liu J, Zenner H (2003) "Fatigue limit of ductile metals under multiaxial loading," Biaxial/Multiaxial Fatigue and Fracture, pp 147–164
25. Böhme S (2022) Tooth flank fracture in spiral bevel gears—multiaxial fatigue and material properties. Dissertation, Technisch-Naturwissenschaftliche Universität Norwegens, Trondheim
26. Niemann G, Winter H, Höhn B-R (2001) Maschinenelemente: Band 1: Konstruktion und Berechnung von Verbindungen, Lagern, Wellen, 3rd edn. Springer, Berlin
27. Hück M (1983) Ein verbessertes Verfahren für die Auswertung von Treppenstufenversuchen. Werkstattstech 24:406–417
28. Pollaschek J (2020) „Fertigungsgerechte Zahnfußoptimierung von Stirnrädern," Diss. RWTH Aachen University, Aachen
29. Lang O-R (1988) Berechnung und Auslegung induktiv randschichtgehärteter Bauteile. Induktives Randschichthärten: 332–349
30. Norm, 2019, "Calculation of load capacity of spur and helical gears—Part 4: Calculation of tooth flank fracture load capacity," ISO/TS 6336-4.
31. Brecher C, Löpenhaus C, Pollaschek J (2017) "Automated defect size determination for gear tooth root bending strength simulation," WIT transactions of engineering. Sciences (116):87–97
32. Van Dang K, Griveau B, Message O (1989) On a new multiaxial fatigue limit criterion: theory and application. Biaxial Multiaxial Fatigue: 479–496
33. Findley WN (1959) A theory for the effect of mean stress on fatigue of metals under combined torsion and axial load or bending. J Eng Ind 81(4):301–305
34. Weber R (2015) „Auslegungskonzept gegen Volumenversagen bei einsatzgehärteten Stirnrädern," Diss., Institut für Werkstofftechnik – Metallische Werkstoffe der Universität Kassel. Universität Kassel, Kassel
35. Simbürger A (1975) Festigkeitsverhalten zäher Werkstoffe bei einer mehrachsigen phasenverschobenen Schwingbeanspruchung mit körperfesten und veränderlichen Hauptspannungsrichtungen. Diss., TH Darmstadt, Darmstadt